Proceedings 10th NUMGE 2023
10th European Conference on Numerical Methods in Geotechnical Engineering
Zdravkovic L, Kontoe S, Taborda DMG, Tsiampousi A (eds)

https://doi.org/10.53243/NUMGE2023-390

The role of hydro-mechanical properties of the tail void grouting material in mechanized tunnelling

D. Mohammadzamani[1], A. A. Lavasan[1], T. Wichtmann[1]

[1] *Department of Civil and Environmental Engineering, Ruhr-Universität Bochum, Germany*

ABSTRACT: Application of tail void grouting material during mechanized tunnelling has an influential effect on hydraulic and stress-deformation regime around the tunnel. In this study, the variation of the hydro-mechanical (HM) properties of the grout has been investigated through 3D Finite Element Method to better understand the interactions around the tunnel under various geological conditions. The model has been validated using available data of the hardening soil small strain (HSS) model. An advanced constitutive model accounting for time-dependent hardening has been assigned to the grouting material. The effect of the parameter variation in the grouting layer on the deformations and excess pore pressures is evaluated using a parametric analysis. According to the results, the hardening rate of the grouting material, compared to other input properties, has the most significant impact on the HM characteristics of the surrounding ground as well as axial forces in the lining.

Keywords: Grouting material, Mechanized tunnelling, Hydro-mechanical properties, Deformation, Excess pore pressure

1 INTRODUCTION

Grouting material in TBM mechanized tunnelling transfers loads and acts as a sealant for the tunnel circumference. Different types of grouting materials are used depending on the geological condition of the excavated ground. Single-component grouts, with setting time lasting up to several hours, are suitable for stable strata, while bi-component grouts, with setting time lasting up to seconds, are used in unstable and water-rich media. During mechanized tunnelling, the stiffness, compressive strength, and permeability of the grouting material are important factors that can significantly affect the stress and deformation regime around the tunnel. However, only a few researchers have conducted studies on the role of grout in numerical simulations of mechanized tunnelling response including the studies done by Lavasan et al. (2018), Lavasan and Schanz (2017), and Kasper and Meschke (2006). These studies mainly focused on singular behaviour of the grout and did not consider all the hydro-mechanical (HM) characteristics of the material in short- and long-term.

This study validates a 3D numerical model of a mechanized tunnel using field measurements of the line 2 Shanghai metro tunnel. The hydro-mechanical properties of the grouting layer are varied using an advanced constitutive model that considers time-dependent stiffness, strain hardening/softening, and other characteristics such as creep, shrinkage, and early age ductility of cementitious material. This elastoplastic model incorporates Mohr-Coulomb failure criterion and Rankine yield surface for deviatoric and tensile loading, respectively. The model also accounts for viscoelastic creep behaviour and isotropic volume loss due to shrinkage (Schaedlich and Schweiger, 2014). The impact of each parameter on deformations and excess pore pressures around the tunnel and the lining response is evaluated.

2 MATERIALS AND METHODS

2.1 Model description and validation

The 6.2 m diameter (D) second line of Shanghai metro tunnel, constructed in 1999 using an Earth Pressure Balance machine, passes through deposited alluvial sediments consisting of mostly silty clay and sand with low permeability values in range of 1×10^{-9} m/s. The tunnel is located at a cover depth of 15 meters with a water level of 1.5 meters below the surface. To monitor pore pressure variation during and after tunnel construction, piezometers were installed around the tunnel (Lee et al., 1999).

To validate deformations and pore pressures over time, a 3D model of the line 2 tunnel was generated using the HSS constitutive model for soil layers (see the properties in Table 1) and the advanced Concrete model for the grouting layer via the PLAXIS 3D code. The Concrete model considers various characteristics such as creep, shrinkage, and early-stage ductility. Input parameters for the Concrete model are listed in Table 2. More information about the HSS and Concrete models can be found in PLAXIS (2021) and Schaedlich and Schweiger (2014). The schematic profile of the tunnel is shown in Figure 1.

Table 1. Parameters of the HSS model for the soil layers in Shanghai metro line 2 (Zakhem and Elnaggar, 2019)

Layer	HSS model parameters				
	E_{50}^{ref} (kPa)	E_{oed}^{ref} (kPa)	E_{ur}^{ref} (kPa)	G_0^{ref} (kPa)	$\gamma_{0.7}$
1	10,000	8,000	30,000	124,000	1.4×10^{-4}
2	1,111	888	7,184	29,000	3.0×10^{-4}
3	942	754	9,165	34,990	3.3×10^{-4}
4	1,525	1,220	7,026	29,270	3.3×10^{-4}
5-1	1,256	1,005	8,898	33,240	3.2×10^{-4}
5-2	1,539	1,231	6,862	28,590	3.2×10^{-4}
6	15,000	12,000	45,000	65,000	3.0×10^{-4}
7-1	20,000	16,000	60,000	75,000	3.1×10^{-4}

In this study, the TBM is simulated using normal pressures acting on the tunnel circumference, resulting from slurry and grout migration along the shield, contributing to deformation control around the tunnel and on the surface (Bezuijen, 2009; Epel et al., 2021). The annulus shield pressure is almost equal to the face pressure ($\pm$5%) with a value of 210 kPa and an incremental depth gradient of 10 kPa/m. The grouting pressure is simulated as a total pore water pressure (Lavasan et al., 2018) acting in the first grouting layer with a value of 220 kPa and a vertical gradient of 20 kPa/m. Segmental linings are generated using Plate structural elements with a length of 1.5 m, thickness of 35 cm, Young's modulus of 31 GPa, and Poisson's ratio of 0.15.

Table 2. Input parameters for the Concrete model representing the grouting material in the model validation

Description (Unit)	**Value**	**Description** (Unit)	**Value**
Young's Modulus, E_{28} (MPa)	500	Tensile fracture energy, G_{t28} (kN/m)	5
Poisson's Ratio, ν	0.2	Equivalent length, L_{eq} (m)	0
Compressive strength, f_{c28} (MPa)	3	Increase of ε_{pcp} with increase of p', a (m)	NA
Tensile strength, f_{t28} (MPa)	2.5	Maximum friction angle, φ_{max} (°)	30
Dilatancy angle, Ψ (°)	0	Ratio between creep and elastic strains, φ_{cr}	NA
Time dependency of elastic stiffness, E_1/E_{28}	0.343	Time for 50% of creep strains, t_{cr50} (days)	NA
Time dependency of strength, $f_{c,1}/f_{c,28}$	0.3	Final shrinkage strain, $\varepsilon\infty_{shr}$	NA
Normalized initially mobilized strength, f_{c0n}	0.15	Time for 50% of shrinkage strains, t_{shr50} (days)	NA
Normalized failure strength, f_{cfn}	0.1	Safety factor for compressive strength, γ_{fc}	1
Normalized residual strength, f_{cun}	0.1	Safety factor for tensile strength, γ_{ft}	1
Uniaxial plastic failure strain at 1, 8, 24 h, ε_{pcp}	NA	Time for full hydration (usually 28 days), t_{hydr}	28
Ratio of residual vs. peak tensile strength, f_{tun}	0	Compressive fracture energy, G_{c28} (kN/m)	80

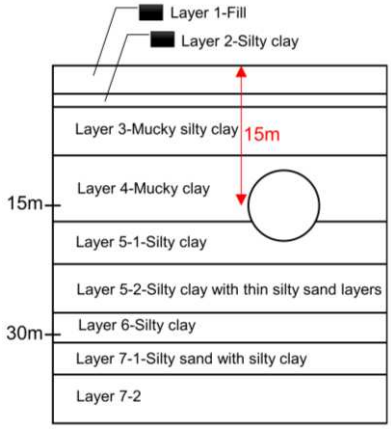

Figure 1. Schematic view of the line 2 metro project and relative soil profiles

Half of the 3D model was used due to symmetry, and boundary conditions were chosen so as not to affect the results. The model boundaries were 8D in the vertical and horizontal directions and 13D in the longitudinal direction. A monitoring section at a distance of 6.5D from the boundary was used to evaluate the results. The top of the model was free from deformations in all directions, the bottom was fully fixed, and the lateral boundaries were normally fixed to allow for in-plane deformations.

The model was calculated using a consecutive scheme, computing all excavation phases using an undrained approach, followed by a consolidation phase for the erection of segmental lining after each TBM advancement. This approach leads to more realistic tunnelling advancement compared to previous research, which considered all phases fully drained or undrained depending on machine speed and ground permeability (Lavasan et al., 2018). The numerical and field data show good agreement and similar behaviour in terms of ground deformation according to Figure 2. In terms of pore pressures measured at the Piezometers installed around the tunnel (Lee et al., 1999), also a complete fit exists between numerical and field data.

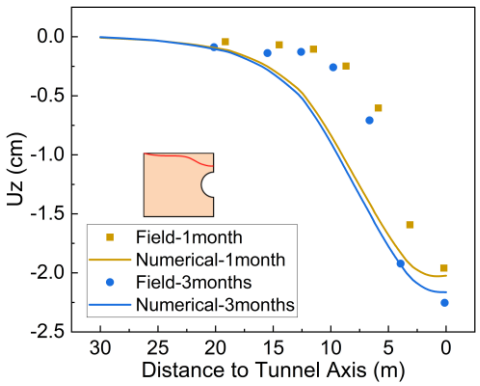

Figure 2. Validation of the numerical model based on the field data for transverse surface settlement

2.2 Parametric analysis of the grout properties

This section evaluates the effect of grouting material's HM behaviour on deformations and hydraulic regime around the tunnel by conducting a parametric analysis. Input values in Table 2 are varied within the range listed in Table 3, and representative results for surface and temporal deformations, excess pore water pressures, and lining response are calculated.

Table 3. Variation of parameters for the Concrete model

Parameter (unit)	Variation Range
Thickness (cm)	7-14-18
Permeability (m/s)	1e-6 to 1e-11
E_{28} (MPa)	500 to 2000
E_1/E_{28} (-)	0.3 to 0.5
Shrinkage strains (%)	0.09 to 5
Creep ratio (-)	1.5 to 2.5

3 RESULTS AND DISCUSSION

3.1 Thickness of the grouting layer

Using Table 3, the grouting layer thickness was varied from 7 to 18 cm to evaluate its effect on the model response. Figure 3 shows surface settlement in the short- and long-term (5.5 days of tunnel construction in the 3D model and 3 months of consolidation after the excavation, respectively) for different thickness values.

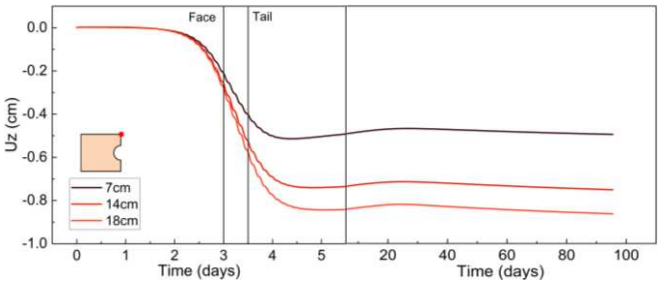

Figure 3. Surface settlement at the monitoring point in short- and long-term based on various thickness of grout layer

The results presented in this figure indicate that an increase in the thickness of the grouting layer results in higher surface settlement values. This can be attributed to the weak mechanical properties of the freshly injected grout, which contribute to the weakness of the tunnel surroundings, leading to higher deformations. However, the long-term values show no significant change in this case, indicating that the thickness of the grouting layer does not affect long-term consolidation deformations on the surface, as the HM properties of the grout have already evolved. Similar behaviour is observed for the crown of the tunnel. Nonetheless, at the invert of the tunnel, long-term deformations differ from short-term values (see Figure 4), which can be attributed to the unloading-induced buoyancy effect resulting from the shield passage (i.e., TBM tail and grout pressure passage at this point).

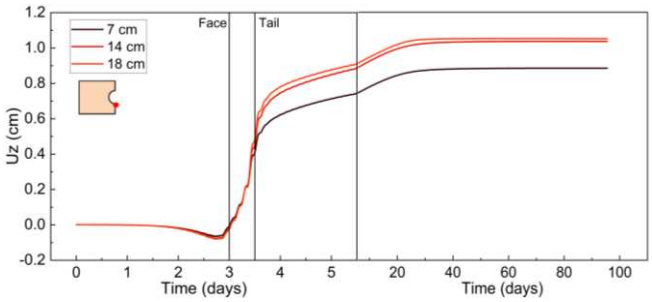

Figure 4. Temporal deformation at invert monitoring point based on various thickness of grout layer

Figure 4 indicates that an increase in the grouting layer thickness leads to higher upward (inward) movements at the tunnel invert. This behaviour can be attributed to the unloading effect caused by the tail passage of the tunnel boring machine, which induces a dilatancy behaviour in the surrounding soil resulting in more pronounced deformations. Furthermore, long-term deformations at the invert are still present for nearly 40 days, in contrast to the tunnel crown and surface. This is due to the existence of unloading-induced excess pore suction, which dissipates after 40 days. The weight effect of the segments controls the deformations at the invert, so unlike the crown, an increase in thickness does not lead to significantly higher deformations. Figure 5 provides a more detailed illustration of this consolidation effect by comparing the generated excess pore water at the tunnel crown and invert.

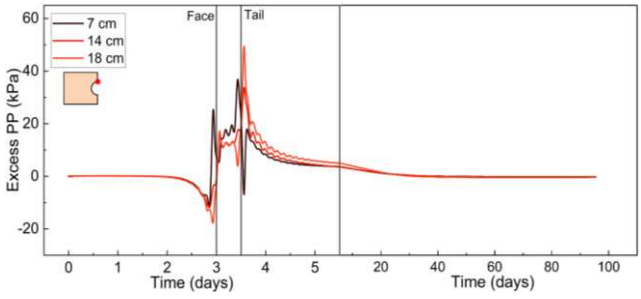

(a)

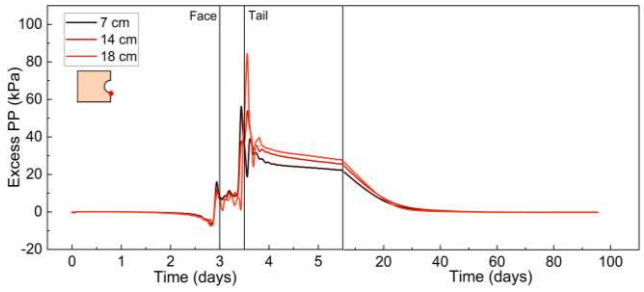

(b)

Figure 5. Generated excess pore water at (a) crown and (b) invert of the tunnel based on various thickness of grout layer

According to Figure 5, the excess pore pressure initially increases before the arrival of TBM, decreases (indicated by positive values in PLAXIS) due to TBM passage and unloading, and then increases again because of the grouting pressure at the TBM tail. Finally, it gradually dissipates with time after the TBM passage. As previously mentioned, positive excess pore water persists at the tunnel invert for almost 40 days after the shield passage (Figure 5(b)), contributing to the remaining long-term deformations after the end of excavation, as observed in Figure 4. The results also indicate that the segmental linings experience higher axial forces (N) at the monitoring section (i.e., 5.5 days after excavation) with an increase in the thickness of the grout layer (Figure 6). This finding is in line with the obtained values for excess pore water and deformations around the tunnel.

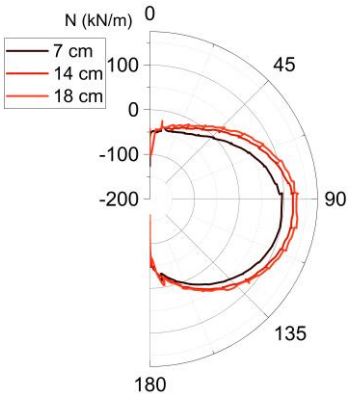

Figure 6. Axial forces in the lining at the monitoring section based on various thickness of grout layer

3.2 HM properties of grouting material

In order to investigate the effect of variation in HM properties of the grouting material on model response, the input variables according to Table 3 has been changed in the 3D model and representative results in terms of deformations and excess pore water regime around the tunnel have been derived in terms of final value (end of excavation - i.e., 5.5 days). The results of the parameter variation on the final surface settlements are presented in Figure 7.

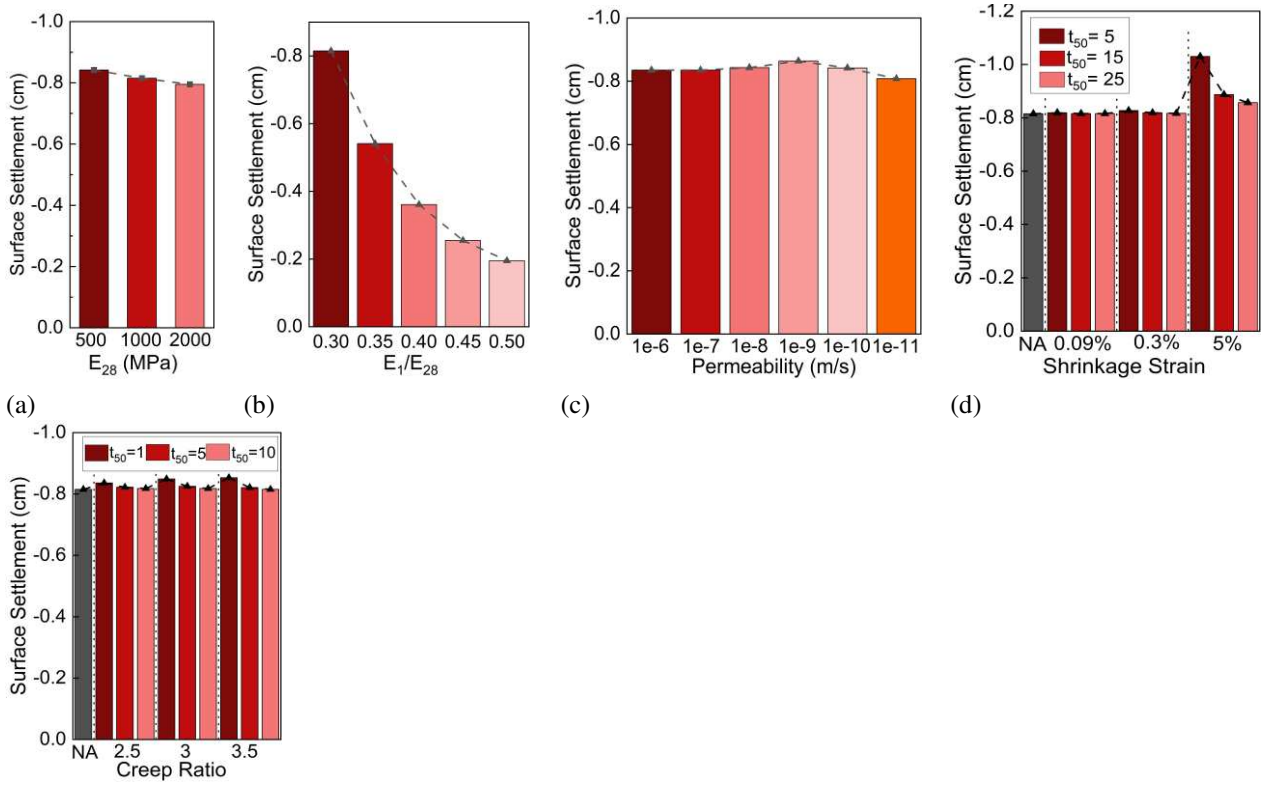

(a) (b) (c) (d)

(e)

Figure 7. Impact of parameter variation in grouting material on surface settlement namely (a) final stiffness (b) hardening ratio (c) permeability (d) shrinkage (e) creep (t_{50} values are in days)

Figure 7 shows that the hardening ratio (E_1/E_{28}) is the only parameter that significantly affects surface settlement, reducing it as it increases. This suggests that a bi-component grout with fast-hardening behaviour can better control tunnel and surface deformations by gaining strength and stiffness in a shorter time. Although the final elastic modulus (E_{28}) also reduces surface settlement when increased, its impact is negligible. Additionally, high shrinkage strains in the short-term (lower t_{50} values) result in more deformation according to Figure 7(d), which evaluates short-term settlements. Similar results were observed for the crown and invert of the tunnel, but due to space constraints, they are omitted, and only the model response for horizontal wall displacement in the tunnel is presented.

The results for horizontal wall deformation show a trend similar to surface settlement values in Figure 7. However, there is a more pronounced difference in final wall deformations due to the buoyancy effect. Increasing the final stiffness of the grout leads to lower deformed tunnel wall (with minor effect similar to the surface) while the hardening ratio has the most significant impact. For slow-hardening grout such as single-component grout (E_1/E_{28}=0.3), the tunnel wall had an inward movement at the end of excavation. In contrast, there is no inward movement in the case of fast-hardening grout (E_1/E_{28}=0.5), meaning that fast-hardened grout would not allow any further deformation after the passage of TBM. The tunnel wall would remain at its outward position (denoted with negative values in this study). The impact of permeability on wall deformation is ambiguous due to the permeability-induced flow direction (Figure 7(c)). When the permeability of the grout is greater than that of the clayey soil, flow occurs towards the grouting layer, resulting in faster dissipation. Conversely, if the permeability of the grout is lower than that of the soil, flow occurs towards the higher permeable soil, leading to slower dissipation and higher wall deformation due to the lower effective stress regime around the tunnel.

Regarding shrinkage in the grout layer, significant wall deformation was observed only for shrinkage strains around 5% and for lower t_{50} values. As this analysis was conducted at the end of excavation (i.e., 5.5 days), low t_{50} values were more pronounced in terms of short-term deformations. However, no specific relationship was observed between creep ratios, representative t_{50} values, and final wall deformation in the tunnel. The only significant deformations were attributed to low t_{50} values, as expected due to the weaker properties of the fresh grout. Longer t_{50} values resulted in a reduced effect of the creep phenomenon.

As for the excess pore water regime (EPP) around the tunnel, since also the trends are similar, only the results for the final excess pore water at the tunnel invert is presented in Figure 8.

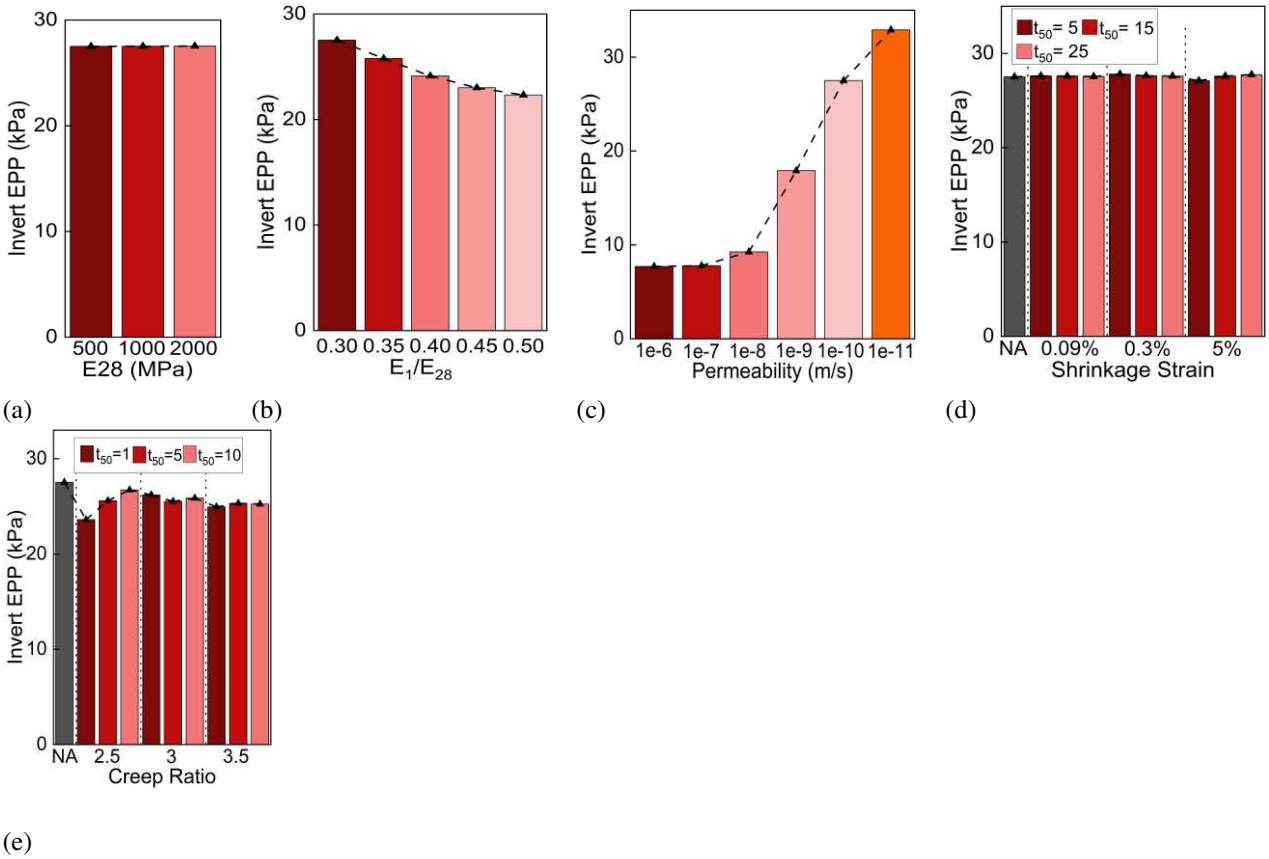

Figure 8. Impact of parameter variation in grouting material on excess pore pressure at invert namely (a) final stiffness (b) hardening ratio (c) permeability (d) shrinkage (e) creep (t_{50} values are in day

Based on Figure 8, the hardening ratio and permeability of the grouting material significantly impact the pore water regime at the tunnel invert and its surrounding areas, with permeability having the greatest influence. Figure 8(b) shows that increasing the hardening ratio decreases excess pore pressure due to the solid phase transition in fast-hardening grout. Conversely, Figure 8(c) indicates that increasing the permeability of the grouting material leads to more excess pore water remaining at the tunnel invert since the tunnel is excavated in soil with low hydraulic conductivity, thus impeding water dissipation. These findings are consistent with those in Figure 4 and 5(b).

In terms of axial forces in the segmental lining at the end of excavation, the impact of parameter variation in the grout layer on the maximum axial forces is also presented in Table 4.

Table 4. Maximum axial forces in the lining as a result of HM property variation of the grout

Property	Range	Maximum N (kN/m)
E28 (GPa)	0.5	125
	1	125
	2	125
Hardening Ratio	0.3	125
	0.35	100
	0.4	50
	0.45	25
	0.5	0
Permeability (m/s)	1.00E-06	130
	1.00E-07	130
	1.00E-08	155
	1.00E-09	155
	1.00E-10	115
	1.00E-11	115
Shrinkage	All	125
Creep	All	150

Table 4 shows that the hardening ratio and permeability of the grouting material significantly affect both the deformations and excess pore water regime around the tunnel, resulting in lower axial forces experienced in the segmental lining. As the hardening ratio increases, lower axial forces are induced in the lining (the bottom part of the segment undergoes almost no axial force in this case) since there is a limit for the deformations and excess pore water dissipation, indicating the effectiveness of fast-hardening grouts such as bi-component grouts in low permeable and saturated media. Conversely, when the permeability of the grout layer is lower than the soil and the flow direction is towards the soil, lower axial forces are also induced in the segmental linings.

4 CONCLUSIONS

Tunnelling in challenging conditions such as high saturated ground, high in-situ pressures, low or high permeable ground as well as soft and unstable media requires careful consideration of the hydro-mechanical characteristics of the tail void grouting material. This study employed a 3D Finite Element Method to investigate the effect of variations in the HM properties of grouting material on the deformations, excess pore water regime, and lining responses. The study found that a thicker grouting layer would lead to higher deformations, excess pore pressures, and long-term (consolidation) deformations. The hardening ratio and permeability of the grouting material were identified as the most influential factors affecting the deformation and excess pore water regime around the tunnel as well as axial forces in the segmental lining. Higher hardening ratios resulted in lower deformations and excess pore pressures around the tunnel, while controlling the induced axial forces in the segmental lining. The permeability of the grouting material affected the value of deformations and excess pore water regime around the tunnel, depending on the flow direction and magnitude of the permeability.

5 Acknowledgements

The first author would like to thank German Academic Exchange Service (DAAD) for the financial support during his PhD research at Ruhr University Bochum, Germany.

6 REFERENCES

Bezuijen, A. 2009. The influence of grout and bentonite slurry on the process of TBM tunnelling, *Geomechanics and Tunnelling* **2.3**, 294-303.

Epel, T. Mooney, M. A, Gutierrez, M. 2021. The influence of face and shield annulus pressure on tunnel liner load development, *Tunnelling and Underground Space Technology* **117**, 104096.

Kasper, T. Meschke, G. 2006. A numerical study of the effect of soil and grout material properties and cover depth in shield tunnelling, *Computers and Geotechnics* **33,** 234-247.

Lavasan, A. A. Schanz, T. 2017. Numerical investigation of hydromechanical interactions at the tail void of bored tunnels due to grouting, *Geotechnical Aspects of Underground Construction in Soft Ground* 161-169.

Lavasan, A. A., et al. 2018. Numerical investigation of tunneling in saturated soil: the role of construction and operation periods. *Acta Geotechnica* **13.3**, 671-691.

Lee, K. M., et al. 1999. Ground response to the construction of Shanghai metro tunnel-line 2. *Soils and Foundations* **39.3**, 113-134.

Schädlich, B. Schweiger, H. F. 2014. A new constitutive model for shotcrete. *Numerical methods in geotechnical engineering* **1**, 103-108.

The Hardening Soil with Small Strain stiffness (HS small). 2021. *In: Material models manual.* PLAXIS 82-94.

Zakhem, A. M. El Naggar, H. 2019. Effect of the constitutive material model employed on predictions of the behaviour of earth pressure balance (EPB) shield-driven tunnels. *Transportation Geotechnics* **21**, 10026